Proceedings of the
Annual Stability Conference
Structural Stability Research Council
San Antonio, Texas, March 19-22, 2024

A beam finite element for tapered and curved members

Rodrigo Gonçalves[1]

Abstract
This paper presents an accurate and computationally efficient beam finite element based on the so-called geometrically exact approach, specifically tailored for non-prismatic beams with thin-walled rectangular section. The element can handle non-linear tapered geometries, initially bent and/or twisted configurations, eccentric loads (loads offset from the centroid), torsion-related secondary (through-thickness) warping and arbitrary primary (membrane) warping, the latter to capture the complex stress field characteristic to tapered and skewed members. To show the capabilities of the proposed finite element, a set of numerical tests are presented. These tests concern 2D/3D linear, linearized buckling and large displacement analyses. For comparison purposes, results taken from the literature or obtained using refined meshes of standard shell finite elements are used.

1. Introduction

Although the structural efficiency and aesthetic qualities of non-prismatic thin-walled beams are widely recognized, their numerical modelling is still quite challenging, a fact that hinders their more widespread use. Such beams can be adequately modelled using shell finite elements, but if local buckling is not a potential failure mode, beam finite elements should be preferable, as they involve much less DOFs and provide structurally meaningful results, such as stress resultants. However, there are several non-trivial effects pertaining to non-prismatic members that must be properly accounted for, namely: (i) variable cross-sections generate stress distributions that can deviate significantly from the standard prismatic beam theory solution and the structural behavior may not be adequately captured by dividing the beam into small prismatic elements, (ii) pre-curved beams exhibit torsion-bending and extension-bending couplings, and (iii) pre-twisted beams are characterized by extension-twist coupling. Although there is a considerable amount of research in this field, it has concerned mostly the lateral-torsional buckling behavior of I-section beams (see e.g. Kitipornchai & Trahair 1972, Ronagh et al. 2000, Andrade & Camotim 2005, Trahair 2014) and the linear in-plane behavior of thin tapered strips (Hodges et al. 2008, 2010, Auricchio et al. 2015, Balduzzi et al. 2016).

In a series of recent papers (Gonçalves 2023a, 2023b, 2024), the author proposed beam finite elements that extend the so-called "geometrically exact beam theory", pioneered by Reissner

[1] Full Professor, CERIS and Universidade Nova de Lisboa, Portugal <rodrigo.goncalves@fct.unl.pt>

(1972, 1973) and Simo (1985), to non-prismatic beams with thin-walled rectangular section. These elements can recover the peculiar stresses in tapered/skewed elements, while handling large spatial displacements and rotations, non-linear taper, pre-twist/bending, torsion-related secondary warping and arbitrary primary (membrane) warping. The present paper summarizes and unifies the work carried out so far and extends it to more general cross-sections (with more walls). The efficiency of the proposed finite element is assessed in a series of numerical tests concerning 2D/3D linear, linear stability (linearized buckling) and large displacement analyses. For comparison purposes, results taken from the literature or obtained using refined meshes of standard shell finite elements are provided.

2. The geometrically exact approach for non-prismatic beams

2.1 Fundamental equations

Consider the narrow rectangular non-prismatic beam shown in Fig. 1, where a parent element-type approach (the reference configuration) is adopted, with $X_2, X_3 \in [-1,1]$, $X_1 \in [-t/2, t/2]$, where t is the cross-section thickness and X_3 corresponds to the beam longitudinal axis. The initial configuration is mapped through

$$\boldsymbol{x}_0 = \boldsymbol{r}_0 + \boldsymbol{\Lambda}_0 \boldsymbol{l}_0, \tag{1}$$

using the position vector $\boldsymbol{r}_0(X_3)$ of the centroid *C*, the cross-section rotation tensor $\boldsymbol{\Lambda}_0(X_3)$ and the cross-section co-rotational vector

$$\boldsymbol{l}_0 = X_1 \boldsymbol{E}_1 + (1+\tau) X_2 \boldsymbol{E}_2, \tag{2}$$

where $\tau(X_3)$ is the taper function. The current configuration is mapped similarly, using

$$\boldsymbol{x} = \underbrace{\boldsymbol{r}_0 + \hat{\boldsymbol{u}}(X_3)}_{\boldsymbol{r}} + \underbrace{\hat{\boldsymbol{\Lambda}}(X_3)\boldsymbol{\Lambda}_0}_{\boldsymbol{\Lambda}} \underbrace{\left(\boldsymbol{l}_0 + \hat{\boldsymbol{l}}\right)}_{\boldsymbol{l}}, \tag{3}$$

in which $\hat{\boldsymbol{u}}(X_3)$ is the displacement of point *C* and $\hat{\boldsymbol{l}}$ allows cross-section warping (displacements along $\boldsymbol{\Lambda}\boldsymbol{E}_3$) through

$$\hat{\boldsymbol{l}} = (\boldsymbol{\omega}^{\mathrm{T}} \hat{\boldsymbol{p}}) \boldsymbol{E}_3, \tag{4}$$

defining amplitudes $\hat{p}_j(X_3)$ and pre-defined warping functions $\omega_j(X_1, X_2)$, stored in a vector format. The rotation tensors are parametrized using the rotation vector ($\boldsymbol{\theta}_0$ for $\boldsymbol{\Lambda}_0$ and $\hat{\boldsymbol{\theta}}$ for $\hat{\boldsymbol{\Lambda}}$), since this allows additive updates and a straightforward geometric interpretation of rotations (Cardona & Géradin 1988, Ritto-Corrêa & Camotim, Gonçalves et al. 2010). The independent kinematic parameters are grouped as follows

$$\hat{\boldsymbol{\phi}} = \begin{bmatrix} \hat{\boldsymbol{u}} \\ \hat{\boldsymbol{\theta}} \\ \hat{\boldsymbol{p}} \end{bmatrix}. \tag{5}$$

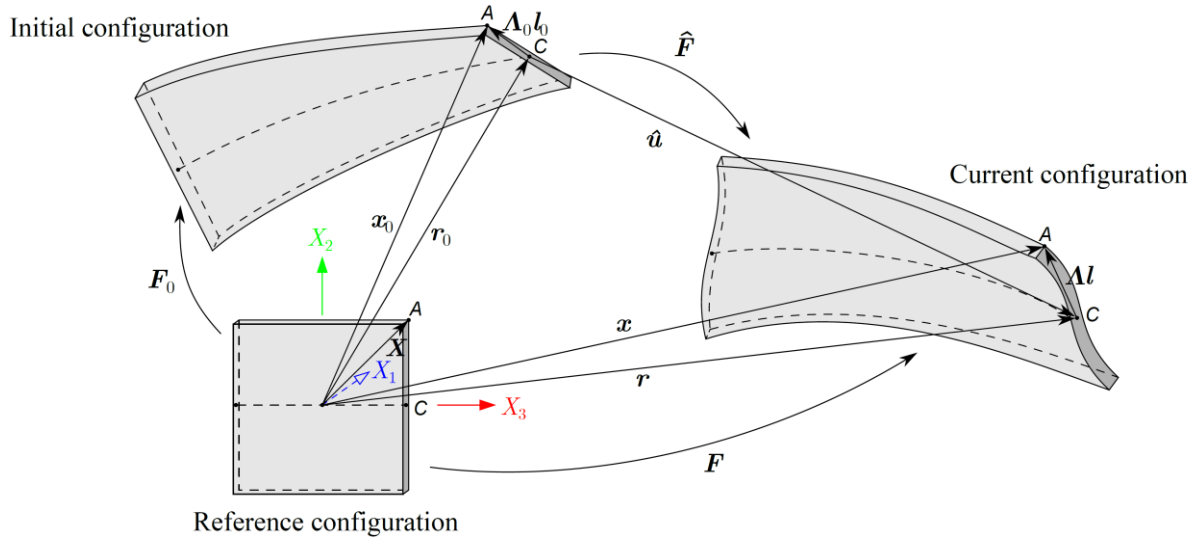

Figure 1: Reference, initial and current configurations of the non-prismatic beam

The three deformation gradients shown in the figure are given by

$$\boldsymbol{F} = \frac{\mathrm{d}\boldsymbol{x}}{\mathrm{d}\boldsymbol{X}} = \boldsymbol{\Lambda G}, \quad \boldsymbol{F}_0 = \frac{\mathrm{d}\boldsymbol{x}_0}{\mathrm{d}\boldsymbol{X}} = \boldsymbol{\Lambda}_0 \boldsymbol{G}_0, \quad \widehat{\boldsymbol{F}} = \frac{\mathrm{d}\boldsymbol{x}}{\mathrm{d}\boldsymbol{x}_0}, \tag{6}$$

with

$$\boldsymbol{G} = \sum_{i=1}^{3} \boldsymbol{g}_i \otimes \boldsymbol{E}_i, \quad \boldsymbol{G}_0 = \sum_{i=1}^{3} \boldsymbol{g}_{0i} \otimes \boldsymbol{E}_i, \tag{7}$$

hence vectors $\boldsymbol{g}_i$ and $\boldsymbol{g}_{0i}$ are back-rotations (by $\boldsymbol{\Lambda}^{\mathrm{T}}$ and $\boldsymbol{\Lambda}_0^{\mathrm{T}}$) of the push-forwards of vectors $\boldsymbol{E}_i$. Since $\widehat{\boldsymbol{F}} = \boldsymbol{F}\boldsymbol{F}_0^{-1}$, the back-rotated Green-Lagrange strains can be written as

$$\begin{aligned} &\widehat{\boldsymbol{E}} = \frac{1}{2}\boldsymbol{\Lambda}_0^{\mathrm{T}}\left(\widehat{\boldsymbol{F}}^{\mathrm{T}}\widehat{\boldsymbol{F}} - \boldsymbol{1}\right)\boldsymbol{\Lambda}_0 = \frac{1}{2}\left(\sum_{i,j=1}^{3}\left(\boldsymbol{g}_i \cdot \boldsymbol{g}_j\right)\boldsymbol{A}_{ij} - \boldsymbol{1}\right), \\ &\boldsymbol{A}_{ij} = \boldsymbol{G}_0^{-\mathrm{T}}\boldsymbol{E}_i \otimes \boldsymbol{E}_j\boldsymbol{G}_0^{-1}. \end{aligned} \tag{8}$$

It turns out that $\boldsymbol{G}_0$ has only five non-null components, viz.

$$G_{11}^0 = 1, \; G_{22}^0 = 1 + \tau, \; G_{j3}^0 = \boldsymbol{g}_{03} \cdot \boldsymbol{E}_j, \tag{9}$$

with $j = 1, 2, 3$, thus $\boldsymbol{G}_0^{-1}$ has an analytical form. After some algebra, it is possible to arrive at the non-null strain components

$$\begin{aligned} \widehat{E}_{13} &= \frac{1}{2}\left(\boldsymbol{\omega}_{,1}^{\mathrm{T}}\,\widehat{\boldsymbol{p}} + \frac{\boldsymbol{E}_1 \cdot \widehat{\boldsymbol{g}}_3^*}{G_{33}^0}\right), \\ \widehat{E}_{23} &= \frac{1}{2}\left(\frac{\boldsymbol{\omega}_{,2}^{\mathrm{T}}\widehat{\boldsymbol{p}}}{G_{22}^0} + \frac{\boldsymbol{E}_2 \cdot \widehat{\boldsymbol{g}}_3}{G_{33}^0}\right), \\ \widehat{E}_{33} &= -\frac{G_{13}^0}{G_{33}^0}\boldsymbol{\omega}_{,1}^{\mathrm{T}}\widehat{\boldsymbol{p}} - \frac{G_{23}^0}{G_{22}^0 G_{33}^0}\boldsymbol{\omega}_{,2}^{\mathrm{T}}\widehat{\boldsymbol{p}} + \frac{\boldsymbol{E}_3 \cdot \widehat{\boldsymbol{g}}_3}{G_{33}^0} + \frac{\widehat{\boldsymbol{g}}_3 \cdot \widehat{\boldsymbol{g}}_3}{2\left(G_{33}^0\right)^2}, \end{aligned} \tag{10}$$

where $f_{,1} = \frac{\mathrm{d}\boldsymbol{f}}{\mathrm{d}X_1}$ and $f_{,2} = \frac{\mathrm{d}\boldsymbol{f}}{\mathrm{d}X_2}$ ($f' = \mathrm{d}\boldsymbol{f}/\mathrm{d}X_3$ will be used next), and

$$\begin{aligned}
&\widehat{\boldsymbol{g}}_3 = \boldsymbol{\Lambda}^{\mathrm{T}}\boldsymbol{F}\boldsymbol{E}_3 - \boldsymbol{\Lambda}_0^{\mathrm{T}}\boldsymbol{F}_0\boldsymbol{E}_3 = \widehat{\boldsymbol{\Gamma}} + \overbrace{\widehat{\boldsymbol{K}} \times \widehat{\boldsymbol{l}}}^{\approx 0} + \widehat{\boldsymbol{K}} \times \boldsymbol{l}_0 + \boldsymbol{K}_0 \times \hat{\boldsymbol{l}} + (\boldsymbol{\omega}^T \widehat{\boldsymbol{p}}')\boldsymbol{E}_3,\\
&\widehat{\boldsymbol{g}}_3^* = \widehat{\boldsymbol{g}}_3 - (\boldsymbol{E}_1 \otimes \boldsymbol{E}_1)\big(\boldsymbol{K}_0 \times \hat{\boldsymbol{l}}\big),\\
&\widehat{\boldsymbol{\Gamma}} = (\boldsymbol{\Lambda}^{\mathrm{T}}\boldsymbol{r}' - \boldsymbol{E}_3) - (\boldsymbol{\Lambda}_0^{\mathrm{T}}\boldsymbol{r}_0' - \boldsymbol{E}_3),\\
&\boldsymbol{K}_0 = \mathrm{axi}(\boldsymbol{\Lambda}_0^{\mathrm{T}}\boldsymbol{\Lambda}_0'),\\
&\widehat{\boldsymbol{K}} = \mathrm{axi}\big(\boldsymbol{\Lambda}_0^{\mathrm{T}}\widehat{\boldsymbol{\Lambda}}^{\mathrm{T}}\widehat{\boldsymbol{\Lambda}}'\boldsymbol{\Lambda}_0\big).
\end{aligned} \tag{11}$$

The use of $\widehat{\boldsymbol{g}}_3^*$, which replaces $\widehat{\boldsymbol{g}}_3$ in $\hat{E}_{13}$, is required to eliminate a recursive relation in the definition of the torsion-related warping function. Indeed, with the simplification and using the Kirchhoff constraint, one readily obtains

$$\hat{E}_{13} = 0 \;\rightarrow\; \omega = \tfrac{X_1 X_2}{G_{33}^0}. \tag{12}$$

A standard Saint Venant-Kirchhoff material law is adopted, hence the second Piola-Kirchhoff stresses $\widehat{\boldsymbol{S}}$ are obtained from

$$\widehat{\boldsymbol{S}} = \boldsymbol{C}\widehat{\boldsymbol{E}},\;\; \widehat{\boldsymbol{S}} = \begin{bmatrix} \hat{S}_{33} \\ \hat{S}_{13} \\ \hat{S}_{23} \end{bmatrix},\;\; \widehat{\boldsymbol{E}} = \begin{bmatrix} \hat{E}_{33} \\ 2\hat{E}_{13} \\ 2\hat{E}_{23} \end{bmatrix},\;\; \boldsymbol{C} = \begin{bmatrix} E & 0 & 0 \\ 0 & G & 0 \\ 0 & 0 & G \end{bmatrix}, \tag{13}$$

with Young's modulus E and shear modulus G. This leads to the equilibrium equations

$$\delta W = -\int_V \delta\widehat{\boldsymbol{E}}^{\mathrm{T}}\,\widehat{\boldsymbol{S}}\,J_0 \mathrm{d}V + \delta\boldsymbol{x}\cdot\boldsymbol{Q} = 0, \tag{14}$$

for the beam reference volume V, the change in volume $J_0 = \det(\boldsymbol{F}_0)$, the concentrated forces $\boldsymbol{Q}$ and the work-conjugate position variations $\delta\boldsymbol{x}$.

2.2 The finite element

It is possible to write the equilibrium equations and their linearization explicitly in terms of the parameters in $\widehat{\boldsymbol{\phi}}$ using the following vector-matrix forms

$$\begin{aligned}
&\delta\widehat{\boldsymbol{E}} = \boldsymbol{\Xi}_{D\widehat{\boldsymbol{E}}}\begin{bmatrix}\delta\widehat{\boldsymbol{\phi}} \\ \delta\widehat{\boldsymbol{\phi}}'\end{bmatrix},\\
&\widehat{\boldsymbol{S}}^{\mathrm{T}}\Delta\delta\widehat{\boldsymbol{E}} = \begin{bmatrix}\delta\widehat{\boldsymbol{\phi}} \\ \delta\widehat{\boldsymbol{\phi}}'\end{bmatrix}^T \boldsymbol{\Xi}_{D^2\widehat{\boldsymbol{E}}}(\widehat{\boldsymbol{S}})\begin{bmatrix}\Delta\widehat{\boldsymbol{\phi}} \\ \Delta\widehat{\boldsymbol{\phi}}'\end{bmatrix},\\
&\delta\boldsymbol{x} = \boldsymbol{\Xi}_{D\boldsymbol{x}}\delta\widehat{\boldsymbol{\phi}},\\
&\Delta\delta\boldsymbol{x} = \delta\widehat{\boldsymbol{\phi}}^T\boldsymbol{\Xi}_{D^2\boldsymbol{x}}\Delta\widehat{\boldsymbol{\phi}},
\end{aligned} \tag{15}$$

where the auxiliary matrices $\boldsymbol{\Xi}_{(.)}$ are provided elsewhere (Gonçalves 2024) and are not displayed here due to lack of space.

A standard isoparametric approach is followed, approximating $\widehat{\boldsymbol{u}}_0$, $\widehat{\boldsymbol{u}}$, $\widehat{\boldsymbol{\theta}}_0$, $\widehat{\boldsymbol{\theta}}$ and $\widehat{\boldsymbol{p}}$ using standard Lagrange polynomials. Besides the torsion-related warping function (12), arbitrary mid-line warping can be included, using Legendre polynomials of degree 2 and above — see Fig. 2, the constant and linear polynomials are linearly dependent to the cross-section motions. Therefore, an element with n nodes and j warping modes has $n(6+j)$ DOFs.

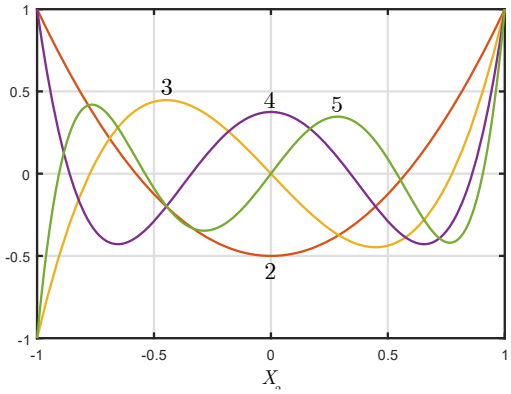

Figure 2: Legendre polynomials of degree 2 to 5

The element interpolation is written as $\widehat{\boldsymbol{\phi}}_e = \boldsymbol{\psi}(X_3)\boldsymbol{d}_e$, where matrix $\boldsymbol{\psi}$ collects the interpolation functions and vector $\boldsymbol{d}_e$ collects the nodal values of the kinematic parameters. This leads to the element internal and external force vectors and tangent stiffness matrix

$$
\begin{aligned}
(\boldsymbol{f}_{int})_e &= \int_V \begin{bmatrix} \boldsymbol{\psi} \\ \boldsymbol{\psi}' \end{bmatrix}^{\mathrm{T}} \boldsymbol{\Xi}_{D\widehat{\boldsymbol{E}}}^{\mathrm{T}}\, \widehat{\boldsymbol{S}}\, J_0 \mathrm{d}V\,, \\
(\boldsymbol{f}_{ext})_e &= \boldsymbol{\psi}^{\mathrm{T}} \boldsymbol{\Xi}_{Dx}^{\mathrm{T}} \boldsymbol{Q}, \\
\boldsymbol{K}_e &= \int_V \begin{bmatrix} \boldsymbol{\psi} \\ \boldsymbol{\psi}' \end{bmatrix}^{\mathrm{T}} \left(\boldsymbol{\Xi}_{D^2\widehat{\boldsymbol{E}}}(\widehat{\boldsymbol{S}}) + \boldsymbol{\Xi}_{D\widehat{\boldsymbol{E}}}^{\mathrm{T}} \boldsymbol{C} \boldsymbol{\Xi}_{D\widehat{\boldsymbol{E}}}\right) \begin{bmatrix} \boldsymbol{\psi} \\ \boldsymbol{\psi}' \end{bmatrix} J_0 \mathrm{d}V - \boldsymbol{\psi}^{\mathrm{T}} \boldsymbol{\Xi}_{D^2x}\, \boldsymbol{\psi}.
\end{aligned}
\tag{16}
$$

Locking is eliminated using reduced Gauss quadrature, with $2 \times k \times (n-1)$ along $X_1 \times X_2 \times X_3$, where k is the greater of 3 and the maximum Legendre polynomial order minus one. It is worth remarking that the MATLAB (2018) implementation of the proposed finite element is very fast. For instance, using ten three-node elements and five warping modes ($n = 3, j = 5$), with an Intel Core i7-8550U CPU @ 1.80 GHz, each iteration takes about 0.06 seconds.

3 Numerical examples

Consistent units are used, with $E = 10^5$ and $\nu = 0.25$. The models using the proposed geometrically exact element always involve uniform discretizations along the length. The error is calculated with $\epsilon = |(a - a_{ref})/a_{ref}|$, where a_{ref} is the reference solution, obtained using refined meshes of standard 2D bilinear solid or MITC shell finite elements (Bathe). Except where stated, the geometries are as defined in Fig. 3.

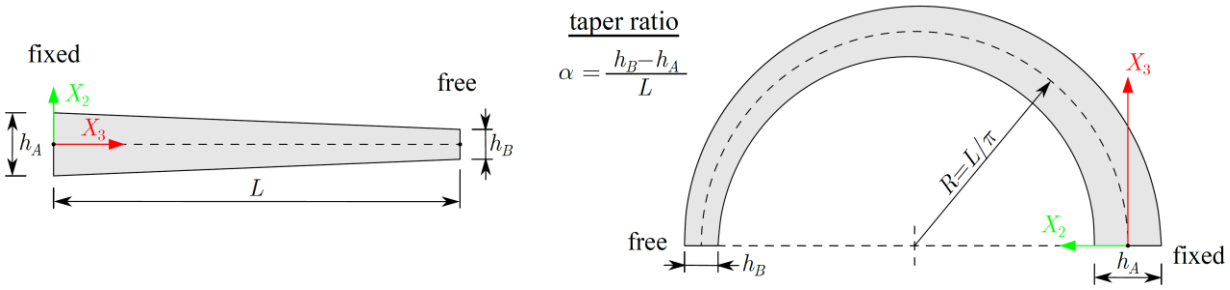

Figure 3: Linearly tapered cantilever geometries.

3.1 In-plane behavior

Figs. 4 and 5 concern geometrically linear analyses of beams undergoing in-plane displacements. In Fig. 4 (linearly tapered straight cantilevers) the reference solutions correspond to (i) 3932160 bilinear elements (Auricchio et al. 2015), for $\alpha = -0.05$, and (ii) 18130 MITC-9 shell elements (Gonçalves 2023a), for $\alpha = -1$. As for Fig. 5 (curved and skewed cantilever), the reference solution was obtained with 262144 bilinear elements (Auricchio et al. 2015). Both these figures show that, naturally, the $n = 4$ element converges at a faster rate, leading to quite accurate displacements for converged meshes: (i) $\epsilon < 0.01$ % for $\alpha = -0.05$, (ii) $\epsilon < 3.0$ % for $\alpha = -1$ and (iii) $\epsilon < 0.08$ % for the skewed case. Note also that the peculiar stress distributions are adequately captured if at least four warping modes are included in the analysis ($j \geq 4$).

A large displacement analysis is carried out for the curved and tapered beam in Fig. 6. The graph shows that, while the horizontal displacement increases with the load, the vertical one increases only up to approximately a 500 load and then decreases. It is concluded that ten $n = 4$ beam elements provide very accurate results even for very large displacements. However, there is a slight improvement if four warping modes are included in the analysis ($j = 4$).

3.2 Linear torsional behavior

The adequacy of the beam element for capturing the torsional behavior in the geometrically linear case is assessed in this section. First, linearly tapered straight cantilevers subjected to a free end torque are analyzed. The results for different taper ratios are presented in Fig. 7. The reference solutions were obtained with refined meshes of MITC-9 shell elements (4000 to 10950 elements, for $\alpha = -0.05$ and -0.5, respectively). Once again, the superior convergence properties of the $n = 4$ element are clearly observed. The errors are quite small for $\alpha = -0.05$ (about 0.5%) but increase with the taper ratio, reaching 4.1% for $\alpha = -0.5$. This can be at least partly explained by the fact that, for $\alpha = -0.5$, the reference (shell) solution exhibits a slight transverse bending near the support which cannot be captured with the proposed element.

Fig. 8 displays the case of a curved and tapered beam subjected by an eccentric out-of-plane force. At least five beam elements including the torsion-related warping function (12) are used, to ensure modeling accurately the initial configuration. This makes $n = 3, 4$ lead to converged and very accurate values for the range shown in the graph, but at least 10 elements are required for $n = 2$. Although not shown in the figure, it is remarked that the warping function of the prismatic beam theory ($G^0_{33} = 1$ in Eq. (12)) leads to completely wrong results, as one obtains $\epsilon = 50.8$ % even with ten $n = 4$ elements.

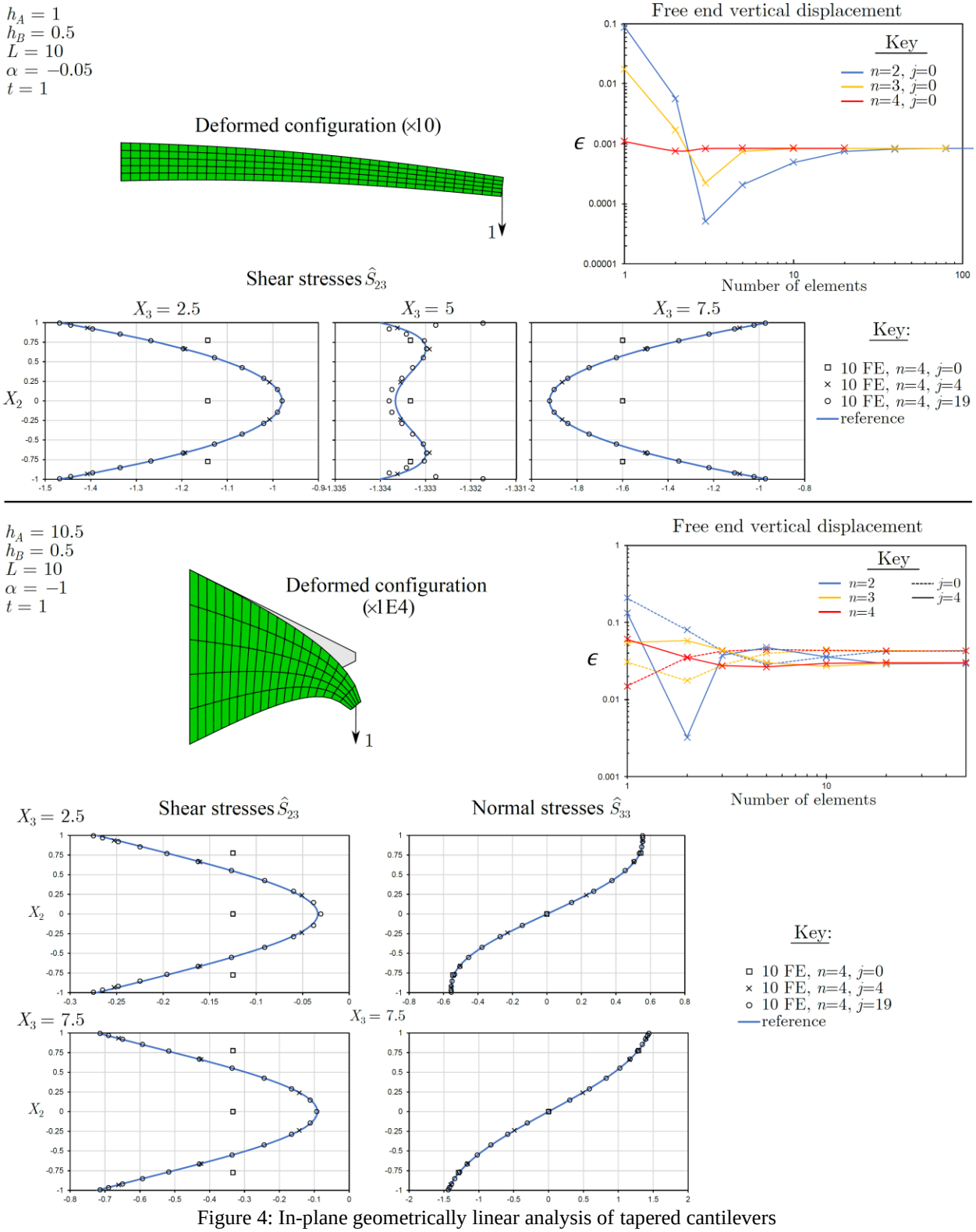

Figure 4: In-plane geometrically linear analysis of tapered cantilevers

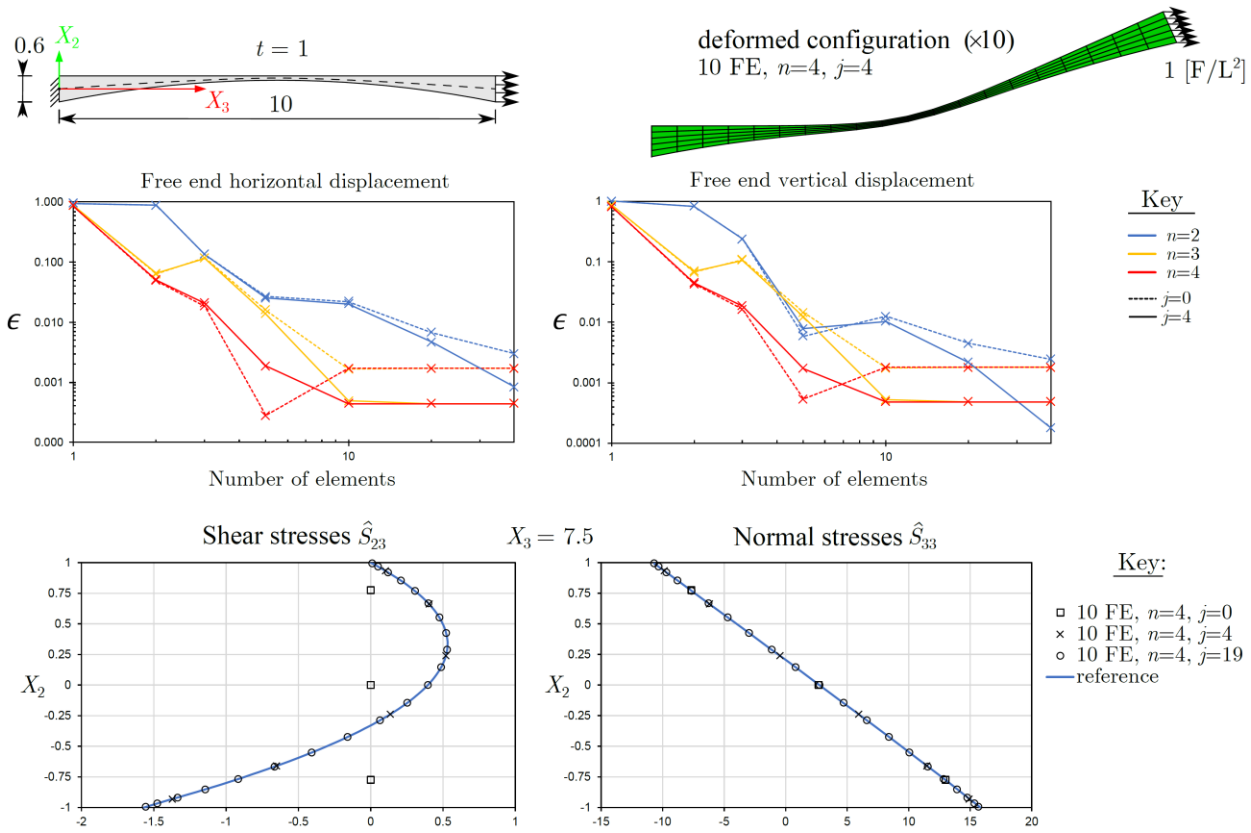

Figure 5: In-plane geometrically linear analysis of a skewed and curved beam

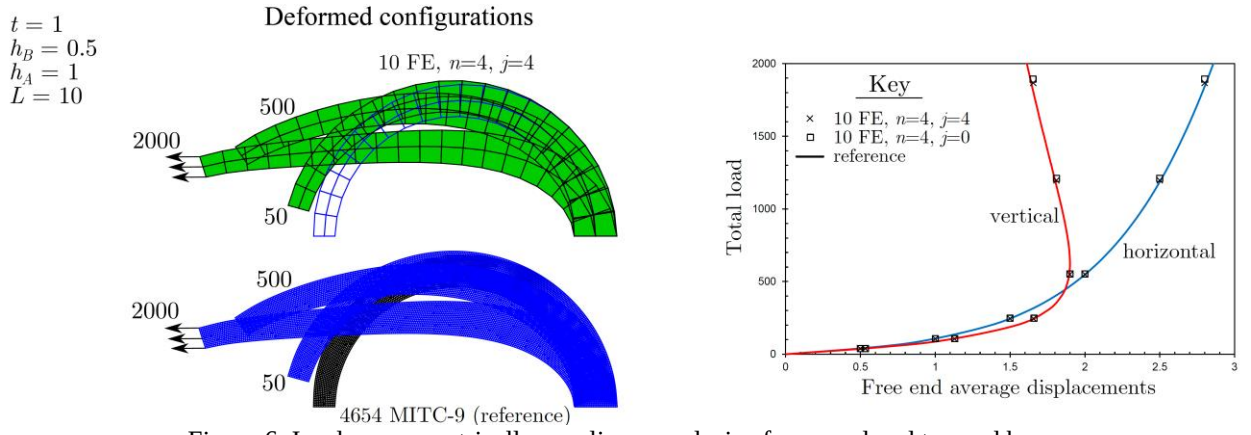

Figure 6: In-plane geometrically non-linear analysis of a curved and tapered beam

3.3 Linear stability analysis

Attention is now turned to the calculation of lateral-torsional bifurcation loads and buckling modes, based on the linear stability analysis concept (pre-buckling deflections are discarded). In all examples, the results obtained with the proposed element correspond to $n = 4$ and $j = 1$ (the torsion-related warping mode), as adding more modes does not change the results obtained. The meshes adopted correspond to converged results.

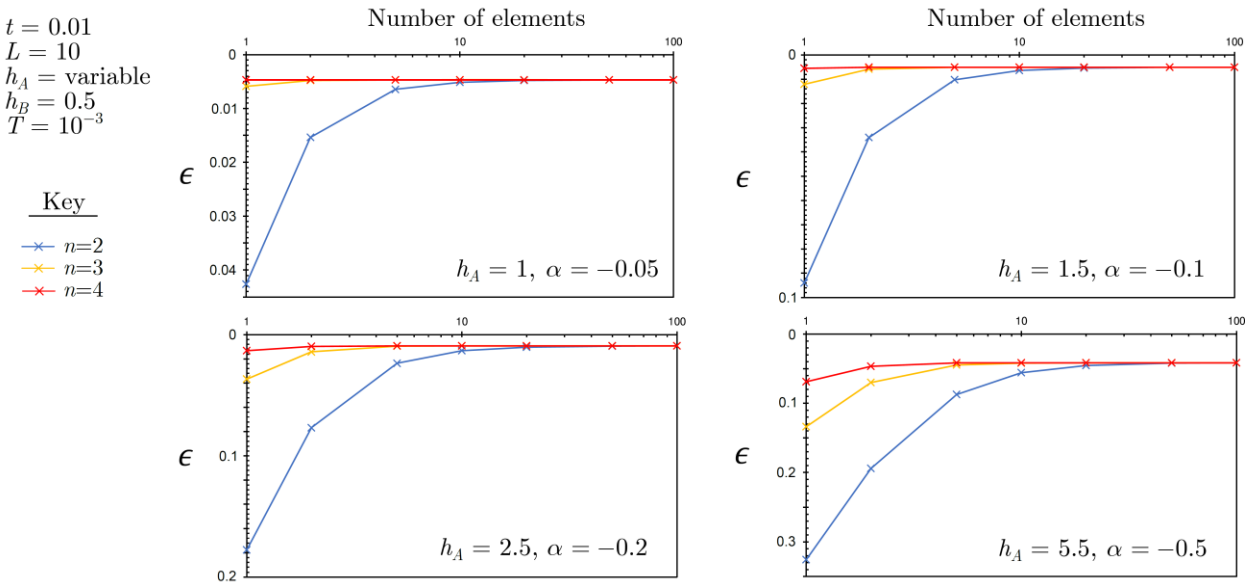

Figure 7: Linear torsion of tapered cantilevers

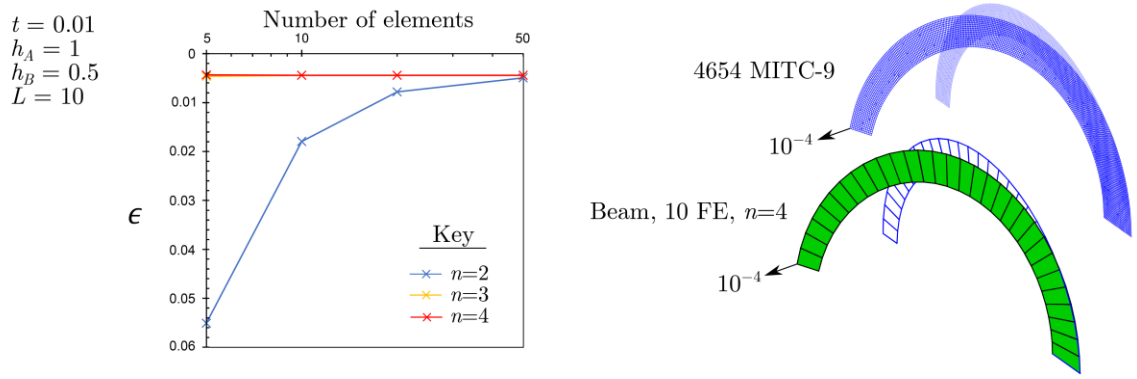

Figure 8: Linear out-of-plane bending-torsion of a curved and tapered cantilever

Fig. 9 shows the critical lateral-torsional buckling modes and the error in the corresponding bifurcation load values, for straight and curved tapered cantilevers subjected to end loads. It can be observed that the buckling modes match very accurately and that the error in the bifurcation loads falls above 2 % only for the highest taper ratio in each case. Note that, in the curved case, the critical buckling mode shapes changes significantly when the load direction changes and that the critical load is much higher for loads directed away from the support.

3.4 Large 3D displacements

Large spatial displacements are considered in this section. All beam results correspond to $n = 3$ and, except where indicated, $j = 1$ i.e. only the torsion-related warping deformation mode is included in the analyses, as adding modes does not change the results.

The extension-twist coupling in linearly tapered pre-twisted beams is examined in Fig. 10. The cantilevers are pre-twisted by 90º and are acted by an axial force, causing the beams to untwist up to 45º. For the maximum rotation, the errors vary between 2.5 and 4.0 %, except for the highest taper ratio ($\alpha = -0.5$), which evidences a much higher value, $\epsilon = 16.3$ %. This can be once more

$t = 0.01$, h_A = variable, $h_B = 0.5$, $L = 10$

Linear taper

ϵ

α	centroid	top	bottom
-0.05	0.07%	0.08%	0.07%
-0.1	0.09%	0.09%	0.08%
-0.2	0.32%	0.33%	0.32%
-0.5	2.6%	2.6%	2.6%

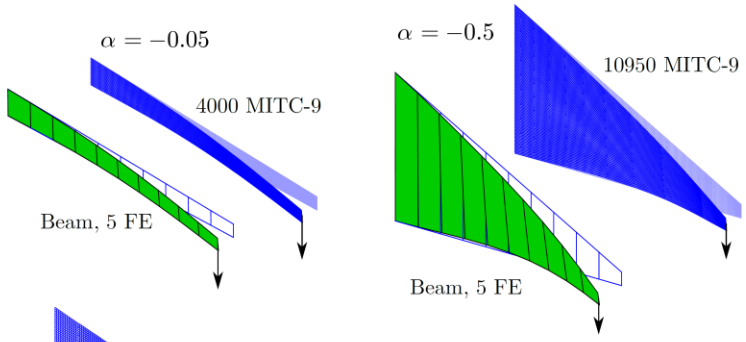

Parabolic taper, $\tau = 0.25 - 0.2X_3 + 0.01X_3^2$

$\epsilon = 0.74\%$
(centroid loading)

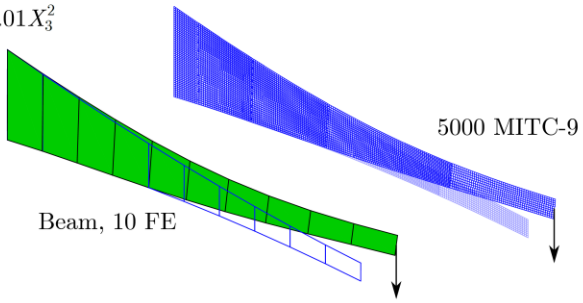

Curved, linear taper

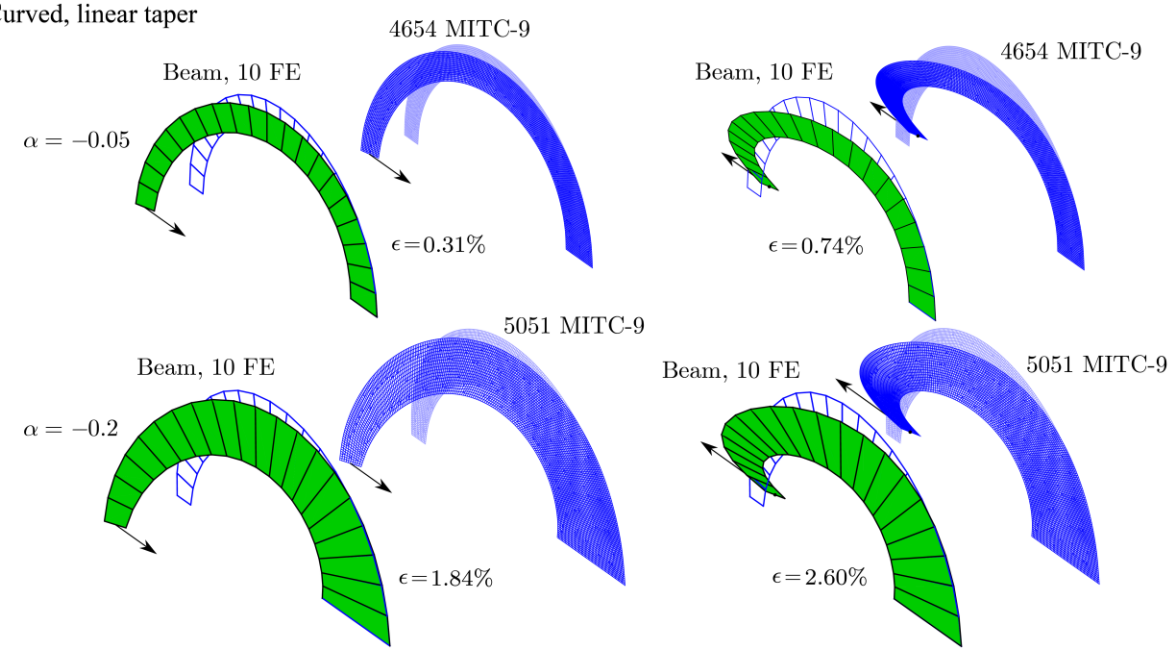

Figure 9: Lateral-torsional critical bifurcation loads and buckling modes for tapered and curved beams

attributed to cross-section transverse bending in the shell model (not captured by the beam model), as increasing the thickness to 0.5 lowers the error to 1.2 %. It is worth noting that increasing α initially leads to a softener structural response — 45º is achieved for lower loads — but the trend is then inverted. This is due to two competing effects that increase with h_A: (i) the torsional stiffness and (ii) the untwisting effect due to axial force.

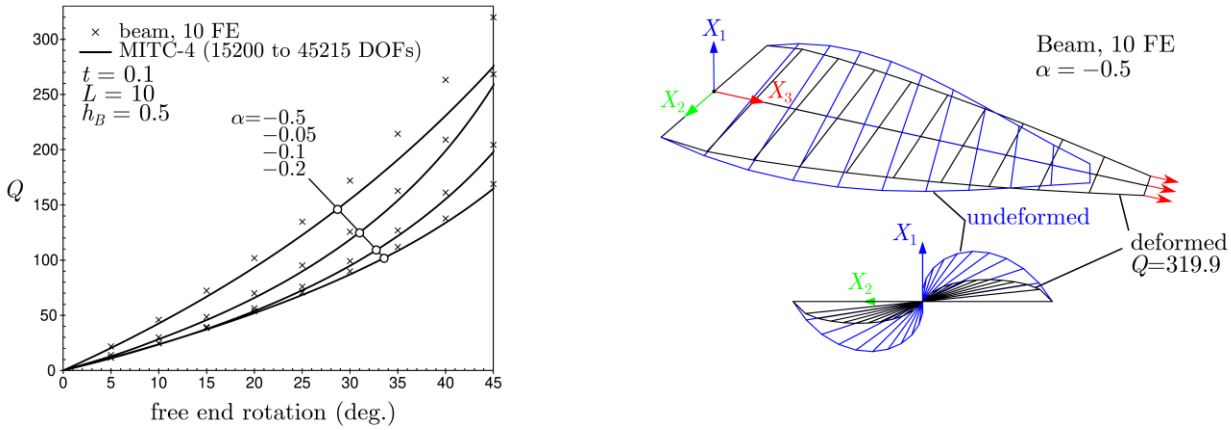

Figure 10: Extension-twist coupling in pre-twisted linearly tapered beams

A set of large displacement problems is presented in Fig. 11. In all cases, $h_B = 0.5$ and $L = 10$. The thickness is set to limit transverse bending: $t = 0.1$ for $\alpha = -0.05$, $t = 0.2$ for $\alpha = -0.2$ and $t = 0.5$ for $\alpha = -0.5$. In the load-displacement graphs, a logarithmic scale is used in the vertical axes to allow a clear perception of the load-displacement path. In all cases an excellent agreement with the reference (MITC-4 shell) solutions is observed, even for very large displacements and finite rotations. However, the accuracy naturally decreases as the taper ratio increases, and it is necessary to add warping deformation modes.

3.5 Beams with multiple walls

The proposed finite element can be combined to model beams with several thin walls. In this case the warping function for all walls must be calculated for a unit twist, which requires substituting (12) by

$$\omega = \frac{X_1 X_2 G_{22}^0}{G_{33}^0}. \tag{17}$$

To illustrate this approach, the cruciform tapered cantilever beam shown in Fig. 12 is analyzed. In the figure, h_C is the total width of the horizontal walls, assumed constant. Ten elements with $n = 4$, $j = 1$ are employed.

For the linear analysis, the error in the vertical displacement of the free end section centroid equals $\epsilon = 0.4\ \%$. The associated critical bifurcation load is subsequently calculated and is also very accurate ($\epsilon = 0.13\ \%$). As shown in the figure, buckling is lateral-torsional.

4 Concluding remarks

This paper summarized recent work in the field of geometrically exact beam finite elements for thin-walled non-prismatic beams (Gonçalves 2023a, 2023b, 2024) and showed that the proposed element can be extended to more general cross-sections (with several walls). The element is capable of handling non-linear taper, initially bent-twisted configurations and eccentric loads. Owing to the geometrically exact description adopted, the element allows obtaining very accurate (i) lateral-torsional bifurcation loads and (ii) equilibrium paths up to very large displacements and

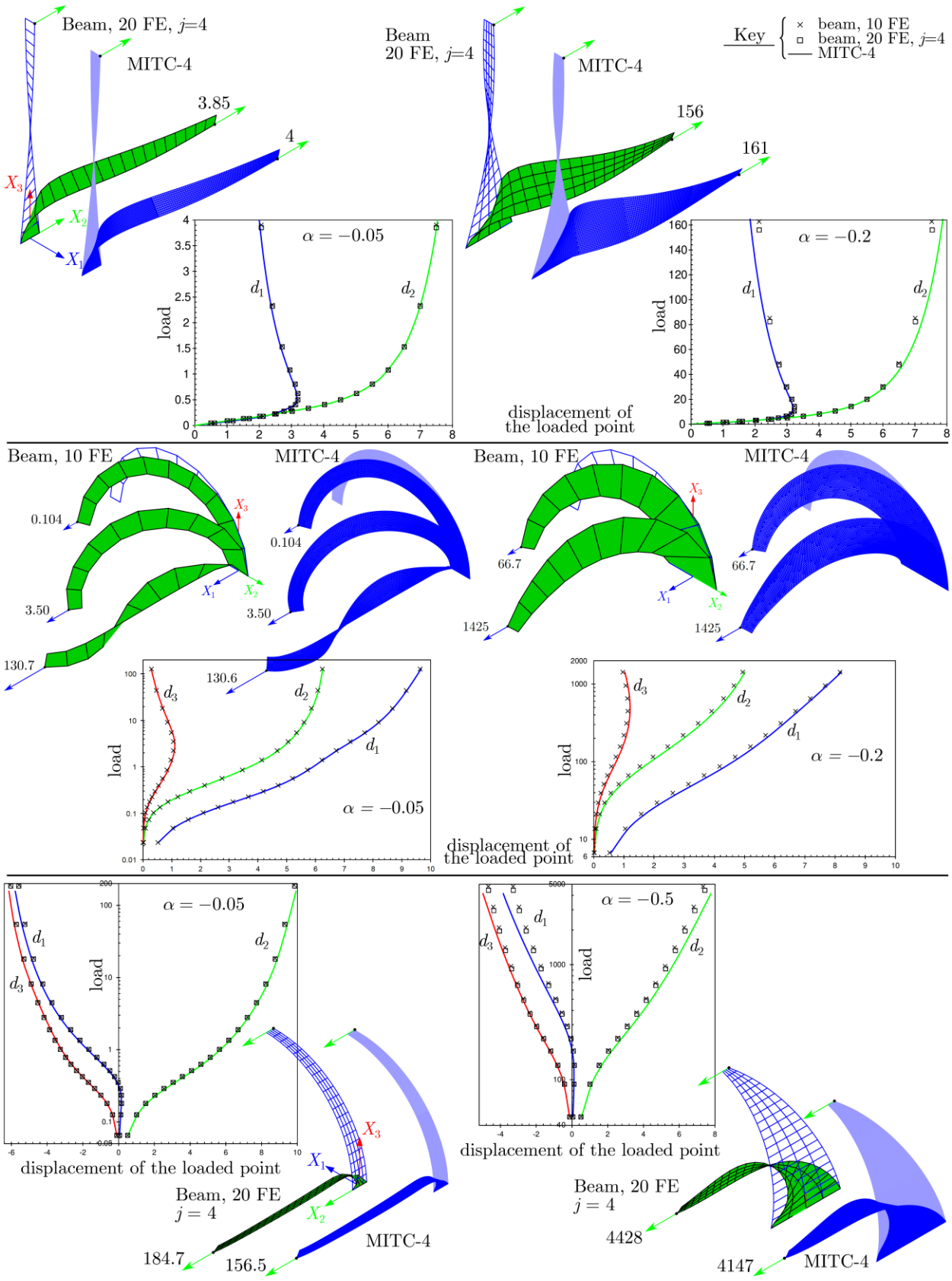

Figure 11: Large spatial displacement analyses of curved and twisted beams

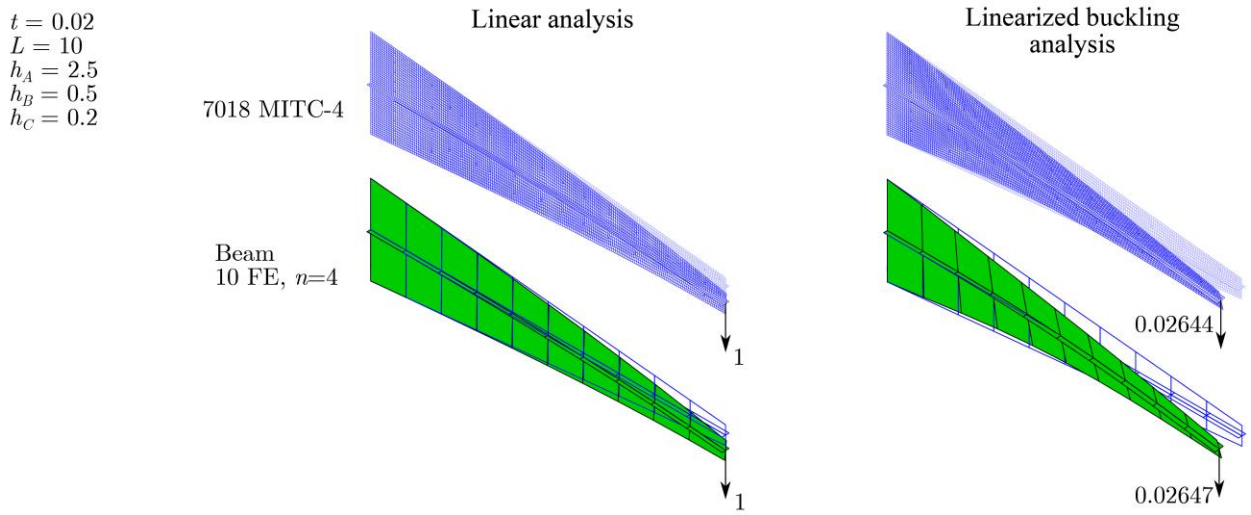

Figure 12: Linear and linear stability analyses of a tapered cruciform beam

rotations. Furthermore, the element allows including hierarchical primary (membrane) warping functions, besides the standard torsion-related secondary (through-thickness) warping, which makes it possible to capture accurately the peculiar stresses that develop in tapered and skewed beams. To demonstrate the performance of the proposed approach, several numerical tests were presented, clearly showing that the beam element allows obtaining accurate solutions with a very small computational cost, even for members with a high taper ratio and initial curvature.

Acknowledgments

This work is part of the research activity carried out at Civil Engineering Research and Innovation for Sustainability (CERIS) and has been funded by Fundação para a Ciência e a Tecnologia (FCT) in the framework of project UIDB/04625/2020.

References

Andrade, A., Camotim, D. (2005). "Lateral-torsional buckling of singly symmetric tapered beams: Theory and applications." *Journal of Engineering Mechanics*, 131(6), 586-597.

Auricchio, F., Balduzzi, G., Lovadina, C. (2015). "The dimensional reduction approach for 2D non-prismatic beam modelling: A solution based on Hellinger–Reissner principle." *International Journal of Solids and Structures*, 63, 264-276.

Balduzzi, G., Aminbaghai, M., Sacco, E., Füssl, J., Eberhardsteiner, J., Auricchio, F. (2016). "Non-prismatic beams: A simple and effective Timoshenko-like model." *International Journal of Solids and Structures*, 90, 236-250.

Bathe, K. J. (2022). *ADINA System*, ADINA R&D Inc.

Cardona, A., Géradin, M. (1988). "A beam finite element non-linear theory with finite rotations." *International Journal for Numerical Methods in Engineering*, 26, 2403-2438.

Gonçalves, R., Ritto-Corrêa M., Camotim D. (2010). "A large displacement and finite rotation thin-walled beam formulation including cross-section deformation", Computer Methods in Applied Mechanics and Engineering, 199(23-24), 1627-1643.

Gonçalves, R. (2023a). "A geometrically exact beam finite element for non-prismatic strip beams: The 2D case." *International Journal of Structural Stability and Dynamics*, 23(4), 2350037.

Gonçalves, R. (2023b). "A geometrically exact beam finite element for non-prismatic strip beams: Linearized lateral-torsional stability." *International Journal of Structural Stability and Dynamics*, 23(12), 2350139.

Gonçalves, R. (2024). "A geometrically exact beam finite element for non-prismatic strip beams: The spatial case." *International Journal of Structural Stability and Dynamics*, available on-line, 245013823.

Hodges, D., Ho, J., Yu W. (2008). “The effect of taper on section constants for in-plane deformation of an isotropic strip.” *Journal of Mechanics of Materials and Structures*, 3(3), 425-440.
Hodges, D., Rajagopal, A., Ho, J., Yu W. (2010). “Stress and strain recovery for the in-plane deformation of an isotropic tapered strip-beam.” *Journal of Mechanics of Materials and Structures*, 5(6), 963-975.
Kitipornchai, S., Trahair N. S. (1972). “Elastic stability of tapered I-beams.” *Journal of the Structural Division*, 98(3), 713-728.
MATLAB (2018), version 9.4.0 (R2018a), The MathWorks Inc., Massachusetts.
Reissner, E. (1972). “On one-dimensional finite-strain beam theory: the plane problem.” *Z. Angew. Math. Phys.*, 23(5), 795-804.
Reissner, E. (1973). “On one-dimensional large-displacement finite-strain beam theory.” *Studies in Applied Mathematics*, 52, 87-95.
Ritto-Corrêa, M., Camotim, D. (2002). “On the differentiation of the Rodrigues formula and its significance for the vector-like parameterization of Reissner-Simo beam theory.” *International Journal for Numerical Methods in Engineering*, 55, 1005-1032.
Ronagh, H., Bradford, M., Attard, M. (2000). “Nonlinear analysis of thin-walled members of variable cross-section. Part I: Theory.” Computers & Structures, 77(3), 285-299.
Simo, J. (1985) “A finite strain beam formulation. The three-dimensional dynamic problem. Part I.” *Computer Methods in Applied Mechanics and Engineering*, 49(1), 55-70.
Trahair, N. (2014). “Bending and buckling of tapered steel beam structures.” *Engineering Structures*, 59, 229-237.